International Journal of Multiphase Flow 130 (2020) 103356

Contents lists available at ScienceDirect

International Journal of Multiphase Flow

journal homepage: www.elsevier.com/locate/ijmulflow

Unraveling low nucleation temperatures in pool boiling through fluctuating hydrodynamics simulations

Francesco Magaletti*, Anastasios Georgoulas, Marco Marengo

Advanced Engineering Center, School of Computing Engineering and Mathematics, University of Brighton, Lewes Road, Brighton BN2 4GJ, UK

ARTICLE INFO

Article history:
Received 23 April 2020
Revised 22 May 2020
Accepted 24 May 2020
Available online 30 May 2020

Keywords:
Boiling
Bubble nucleation
Fluctuating hydrodynamics
Diffuse interface model

ABSTRACT

When dealing with numerical simulations of boiling phenomena, the spontaneous appearance of vapor bubbles is one of the most critical feature to be addressed. Capturing bubble formation during the dynamics, instead of patching vapor regions as initial conditions, is crucial for the correct evaluation of nucleation rates and nucleation site density, two of the most important parameters characterizing boiling. In this work the Diffuse Interface modeling for vapor–liquid systems is coupled with Fluctuating Hydrodynamics Theory to properly address this aspect and to analyze the detailed nucleation mechanism during boiling inception on a hot surface. The simulations revealed a new enhancing mechanism of bubble formation that is able to explain the low onset temperature measured in boiling experiments on ultra-smooth, wettable surfaces: the interaction and coalescence between sub-critical vapor embryos plays a fundamental role in lowering the onset temperature, increasing the lifetime of the embryos and their probability to trigger the phase change.

1. Introduction

Being one of the most efficient modes of heat transfer, boiling is used in several applications such as electronics cooling, chemical processes, fuel cells, etc. Phase changing systems, which exploit the large latent heat associated with phase change, are representing an innovative route to enhance heat transfer or storage of thermal energy. Micro-channel flow boiling constitute a suitable example of such technologies, exploiting evaporation to increase the heat transfer (Kandlikar, 2004). From a technological point of view, a suitable cooling system should work within the nucleate boiling regime, at the highest possible value of the heat transfer coefficient (HTC) without crossing the critical heat flux (CHF) condition, after which a burn-out occurs with a sudden increase of the surface temperature associated with a decrease of the HTC (Dhir, 1998). The ideal solution is to anticipate the onset of nucleate boiling (ONB) as much as possible by reducing the onset temperature (i.e. the temperature at which the bubbles start appearing at the hot surface), and to delay the CHF condition by increasing the maximum HTC. Its implementation, however, faces a number of challenges and requires solution to several fundamental problems. In any practical application the boiling efficiency depends on parameters, such as the frequency of bubble nucleation, their size, and the release rate from the hot surface. One of the most stimulating and intriguing problems is the prediction of the onset temperature. It is in fact well known that a liquid can be kept at a temperature higher than the boiling point without forming any vapor bubble, the so-called *superheated* condition (or, more generally, *metastable state*) (Carey, 2018). The level of heat flux, the thermodynamic condition of the liquid (temperature and pressure), the surface material and finish, and the presence of impurities dissolved into the liquid all have an effect on the conditions at which boiling occur (Incropera et al., 2007).

Nowadays our understanding of the nucleation phenomena is mainly built upon quasi-static descriptions like the one provided by the Classical Nucleation Theory (CNT) (Blander and Katz, 1975). CNT poses the basis for the theoretical modeling by means of simple energy arguments and allows the estimation of energy barriers and nucleation rates in homogeneous conditions. Other more fundamental approaches like Density Functional Theory (DFT) (Oxtoby and Evans, 1988; Shen and Debenedetti, 2001) and CNT extensions (Lutsko and Durán-Olivencia, 2015; Lutsko, 2018) have been proposed, addressing and correcting some CNT expectations. Alternatively, brute force Molecular Dynamic (MD) simulations represents a powerful, but computationally expensive, tool to address nucleation processes (Diemand et al., 2014; Novak et al., 2007). CNT can also be easily extended to heterogeneous cases, in the idealized condition of a perfectly smooth surface (Ward et al., 1983), providing a simple theoretical framework to take into account wall

* Corresponding author.
E-mail address: F.Magaletti@brighton.ac.uk (F. Magaletti).
URL: https://research.brighton.ac.uk/en/persons/francesco-magaletti (F. Magaletti)

https://doi.org/10.1016/j.ijmultiphaseflow.2020.103356
0301-9322/© 2020 Published by Elsevier Ltd.

wettability. The heterogeneous nucleation is believed to be the most effective mechanism for the inception of phase transformation, since solid walls and impurities enhance the formation of a new thermodynamic phase, reducing the activation energy requested for the phase change and, consequently, reducing the onset temperature. However CNT predicts substantially lower superheats, with respect to the homogeneous case, only close to poorly wettable surfaces, characterized by high value of the contact angle. For real systems and applications, however, the contact angle is rarely greater than 110^o and, most often, significantly lower than 90^o since organic liquids wet extremely well metallic surfaces. In these conditions CNT predicts a superheat level which is only slightly smaller than the corresponding homogeneous nucleation. Wall temperatures on the order of 300^{o}C, for example, would be necessary to observe water boiling at atmospheric pressure if the theory were correct. On the contrary, superheats of no more than $15-20^o$C are usually required in real conditions, mostly depending on the surface roughness (Bourdon et al., 2015). The main mechanism which is able to explain such low superheat levels is the gas/vapor entrapment in the imperfections of the solid surface, which is usually characterized by an heterogeneous distribution of cavities with different size such as machine-formed pits, scratches and irregularities. Gas or vapor remain trapped into these cavities during the liquid filling of the system and, later, act as a catalyst for bubble nucleation (Carey, 2018).

Despite the arguments provided by the cavity theory sound logical and find confirmation in experiments (Lorenz et al., 1974; Cornwell, 1977; Wang and Dhir, 1993), recent studies (Qi and Klausner, 2006; Theofanous et al., 2002; Bourdon et al., 2015) show that the entrapment mechanism inside the cavities is not the only responsible for the low superheat level measured in the experiments. They found superheats as low as 10^{o}C even on ultra smooth surfaces, with a mean roughness of few nanometers. According to the cavity theory, nanometric cavities would require superheats on the order of homogeneous nucleation, in contrast with the recent accurate experimental results. Contradictions in different experiments and theoretical mis-prediction show that a complete understanding of the nucleation mechanism close to the hot wall is still lacking and further research is required. The experimental protocols and the characterization methods of the surfaces before the boiling measurements play a critical and, sometimes, unexpected role on the obtained results. The experiments by Theofanous et al. (2002), performed on nano-film heaters allow to remove the issue of microscopic roughness and the effects of nonuniform heat fluxes. They characterized their surfaces through AFM and SEM analysis, obtaining an rms roughness of 4nm, and observed nucleation at $4-7^o$C superheat. They observed that aged and fresh surfaces behave differently, with a higher nucleation site density measured on aged surfaces (up to one order of magnitude). Moreover, at very low superheat, they observed a nonuniform spatial distribution of the nucleation sites, maybe suggesting a non uniformity of the chemical properties of the surface. Notably, Frenkel in his early works in the '40s already proposed the idea that inhomogeneities can be responsible for heterogeneous nucleation (Frenkel, 1955), introducing the concept of *Frenkel's island*, poorly wettable microscopic patches due to impurities and/or surfactants. Majumdar and coworkers proposed that nano-film instability could anticipate heterogeneous nucleation (Majumdar and Mezic, 1999). They showed, in condensation experiments, that water films with a thickness between $3-10$nm are unstable and that the rupture of this layer produces water droplet. This mechanism could be effective in condensation since most of the metallic surfaces used in applications are hydrophilic, hence water molecules are absorbed close to the interface; the disjoining pressure in this conditions plays a crucial role. However, when the reasoning is transposed to vapor bubble formation, it could not explain the measured value of superheat, since it would require strongly hydrophobic surfaces to repel water molecule far from the surface and to create these unstable films. MD simulations by Kimura and Maruyama (2002) addressed this problem and do not confirm the nucleation scenario proposed by Majumdar.

These observations open questions and call for new paradigms and mechanistic models in order to gain a better understanding of the complex phenomena occurring during nucleation and boiling. With the increase of computational power and the recent development of more accurate multiphase flow models, numerical simulations are becoming an extremely valuable and effective tool for the analysis of boiling (Dhir et al., 2013). However, among the three modes of boiling (nucleate, transition and film boiling) film boiling is the most suitable for this kind of analysis due to the presence of the two-phase flow from the very initial condition. Most of the numerical techniques addressing boiling, in fact, requires that bubbles or a vapor film are patched inside the liquid system when the simulation starts. Lee and Nydahl (1989) initialized the system with a bubble of radius 2μm in contact with the hot surface and followed the bubble growth up to its departure. A similar approach has been used also in Patil and Prusa (1991). An improvement has been possible with the advent of the numerical tracking methods. In particular, Welch (1998) adapted a front tracking technique to cope with the additional difficulties posed by the vapor bubble growth problem. One major issue is that the interface is not simply advected by the fluid velocity, since the evaporation produces a velocity jump between the liquid and the vapor phase. Another point is represented by the high resolution required close to the interface in order to accurately capture the thermal gradients and, as a consequence, the correct mass transfer rate. Other possible approaches are represented by interface capturing techniques such as the Level Set (LS) method modified to take into account the phase change at the liquid-vapor interface (Son et al., 1999; Lee and Son, 2017). Another similar approach is the Volume of Fluid (VOF) method which has been applied for the simulation of boiling heat transfer (Kunkelmann and Stephan, 2009) and to characterize the bubble growth and detachment in pool boiling (Georgoulas et al., 2017). Many of these model divide the geometrical domain into parts around a growing bubble using different transfer models for the so-called micro- and macro- regions (Son et al., 1999). In other cases they simplifies the problem assuming saturation conditions or thermodynamical equilibrium within the vapor bubble (Welch, 1998). The Lattice Boltzmann approach has been proposed to avoid these simplifying assumptions (Hazi and Markus, 2009; Gong and Cheng, 2013), but introduces the requirement of a collision operator (the Bhatnagar–Gross–Krook is often chosen) and of the interaction potential between the solid and the fluid to model wettability. Furthermore, all the previously cited methods assume some closure relation to estimate the evaporating mass flux as a function of the temperature gradient at the interface, the latent heat of vaporization, and other parameters. In order to avoid these closure relations, a thermodynamically consistent modeling of the two-phase flow has been proposed within the context of the Diffuse Interface approach (Liu et al., 2015). This methodology describes the liquid-vapor interface down to a nanometric length scale and naturally embeds capillarity and phase change with the associated latent heat.

All these numerical studies contributed to increase our understanding of the controlling parameters for bubble growth and departure. However, they refer to the dynamics of the bubble growth ones it has formed. The vapor nuclei need to be prescribed instead of being captured by the solution, with the risk of altering the nucleation rate and the nucleation site density. When dealing with boiling onset simulations the still open challenge is, instead, to let the nuclei spontaneously appear, like it happens at the phase change inception, with a physically-grounded methodology captur-

ing the proper statistical properties. At the moment, MD is the only universally trusted tool for such a task, but its enormous computational cost limits its use only to fundamental study (Diemand et al., 2014), making it not viable for engineering-oriented simulations. Recently a promising approach based on the coupling of Fluctuating Hydrodynamics Theory and Diffuse Interface modeling (Gallo et al., 2018; 2020) proved to be effective when dealing with bubble nucleation. Compared with MD simulations, this mesoscopic approach gives access to much larger systems at a much cheaper computational cost. Moreover it enables the spontaneous nucleation of vapor bubbles in metastable quiescent liquid thanks to the proper description of thermal fluctuations.

The aim of the present work is to numerically analyze the boiling inception phenomenon, addressing the detailed mechanisms underlying the vapor bubble formation and gaining new insights for the surprisingly low superheat level measured in the experiments on ultra-smooth surfaces. The Fluctuating Diffuse Interface approach will be extended to boiling conditions for this analysis. The paper is structured as follows: in Section 2 the mathematical model will be thoroughly described; Section 3 will be devoted to the numerical and algorithmic aspects; In Section 4 the simulations results will be analyzed and discussed; finally, the conclusions and a discussion on still open questions will be drawn in Section 5.

2. Mathematical model

In this section the mathematical model exploited in this work will be reviewed. The description of the two–phase, vapor–liquid, system is addressed through a diffuse interface approach. This is particularly effective when dealing with fluid systems at submicron scales, since it allows to capture the detailed properties of a vapor–liquid interface, down to the molecular scale. Fluctuating Hydrodynamics theory is built upon the diffuse interface modeling in order to address thermal fluctuations in a continuum setting. Fluctuations are the triggering mechanism for any nucleation event in metastable systems, hence it is crucial to properly model them in a thermodynamically consistent way.

2.1. The diffuse interface description of vapor–liquid systems

The Diffuse Interface (DI) modeling of vapor–liquid systems dates back to van der Waals (see the english translation by Rowlinson of his seminal work in Van der Waals, 1979), but could be rephrased in a more modern language within the framework of Density Functional Theory (Lutsko, 2011). This approach is able to capture the steep, but continuous, density field variation occurring at molecular scale across a vapor–liquid interface. As a result, capillary effects (i.e. the surface tension) naturally emerge from the modeling. This is one of the major differences with the more classical Gibbs-like approaches, where a sharp surface associated with a suitable energy density separates the two distinct phases. When looking at the thermodynamic descriptions of the two–phase system, in particular the Helmholtz free energy expression, the differences are apparent: on one hand, the sharp interface approach provides a model explicitly in terms of the interface area, $F = -p_L V_L - p_V V_V + \gamma A$ with the subscripts L, V indicating the liquid and vapor phases, respectively, p the pressure, V the volume, γ the surface tension and A the interface area; on the other hand the diffuse interface approach adopts a description in terms of the spatially varying density and temperature fields, producing a Helmholtz free energy functional

$$F[\rho,\theta] = \int_{\mathcal{D}} \left[f_b(\rho(\mathbf{x}),\theta(\mathbf{x})) + \frac{\lambda}{2}|\nabla\rho|^2 \right] \mathrm{d}V, \tag{1}$$

where $\mathcal{D}$ is the entire fluid domain, $\rho(\mathbf{x})$ is the density field, $\theta(\mathbf{x})$ is the temperature field, f_b is the classical bulk free energy density (per unit volume) of a homogeneous fluid at density ρ and temperature θ, namely the Equation of State describing the thermodynamic properties of the specific fluid. Finally, the square gradient term, multiplied by the so-called capillary coefficient λ, energetically penalizes density spatial variations and, in particular, the formation of interfaces between two regions at different density (Lutsko, 2011; Espanol, 2001; Jamet et al., 2001; Magaletti et al., 2015). The other thermodynamic properties are consistently obtained through derivatives of the bulk free energy density, for example the pressure $p = \rho^2 \partial(f_b/\rho)/\partial\rho$, or the entropy density $s_b = -\partial f_b/\partial\theta$. In the diffuse interface approach the interfacial properties, namely the surface tension γ and the interface thickness ϵ, directly results from the choice of the Equation of State ($f_b(\rho, \theta)$) and of the coefficient λ (see Magaletti et al. (2016) for details) as:

$$\gamma(\theta) = \int_{\rho_V^{sat}(\theta)}^{\rho_L^{sat}(\theta)} \sqrt{2\lambda\left[\omega_b(\rho,\theta) - \omega_b(\rho_V^{sat}(\theta),\theta)\right]}\,\mathrm{d}\rho\,, \tag{2}$$

$$\epsilon(\theta) = \left[\rho_L^{sat}(\theta) - \rho_V^{sat}(\theta)\right] \sqrt{\frac{\lambda}{2\left[\omega_b(\bar\rho) - \omega_b(\rho_V^{sat})\right]}}\,. \tag{3}$$

In the above equations $\omega_b(\rho,\theta) = f_b(\rho,\theta) - \mu_b(\rho,\theta)\rho$ is the Landau free energy density, $\mu_b(\rho,\theta) = \partial f_b/\partial\rho$ is the chemical potential and $\rho_{V/L}^{sat}(\theta)$ are the temperature dependent vapor and liquid densities at saturation, respectively. Finally, in the interface thickness expression, $\bar\rho$ is the density where ω_b achieves a local maximum at fixed temperature, with $\rho_V^{sat} < \bar\rho < \rho_L^{sat}$. As shown in Gallo et al. (2018), once the Equation of State has been chosen, a constant value of λ is sufficient to reproduce the correct temperature dependence of the surface tension of the chosen fluid.

Following the procedure of nonequilibrium thermodynamics (De Groot and Mazur, 2013), the description is straightforwardly extended to dynamic conditions. New stress and energy flux contributions arise from the capillary term in the free energy functional, Eq. (1). As a result, a modified set of Navier–Stokes equations enforcing mass, momentum and energy conservations is obtained (Magaletti et al., 2016; Jamet et al., 2001):

$$\begin{aligned} \frac{\partial\rho}{\partial t} + \nabla\cdot(\rho\mathbf{u}) &= 0\,,\\ \frac{\partial\rho\mathbf{u}}{\partial t} + \nabla\cdot(\rho\mathbf{u}\otimes\mathbf{u}) &= \nabla\cdot\boldsymbol{\tau}\,,\\ \frac{\partial e}{\partial t} + \nabla\cdot(\mathbf{u}e) &= \nabla\cdot(\boldsymbol{\tau}\cdot\mathbf{u}) - \nabla\cdot\mathbf{q}\,, \end{aligned} \tag{4}$$

where $\mathbf{u}$ is the fluid velocity;

$$\boldsymbol{\tau} = -p\boldsymbol{I} + \mu\left(\nabla\mathbf{u} + \nabla\mathbf{u}^T\right) - \frac{2}{3}\mu\nabla\cdot\mathbf{u}\boldsymbol{I} + \\ +\lambda\left(\frac{1}{2}|\nabla\rho|^2 + \rho\nabla^2\rho\right)\boldsymbol{I} - \lambda\nabla\rho\otimes\nabla\rho$$

is the stress tensor augmented with the diffused capillary stresses (in the second row), with μ the dynamic viscosity of the fluid (in general, a function of both density and temperature);

$$e = \mathcal{U}_b + \frac{1}{2}\rho|\mathbf{u}|^2 + \frac{\lambda}{2}|\nabla\rho|^2$$

is the total energy density, with $\mathcal{U}_b = f_b + \theta s_b$ the bulk internal energy density; finally

$$\mathbf{q} = -k\nabla\theta + \lambda\rho\nabla\cdot\mathbf{u}\nabla\rho$$

is the energy flux augmented with a capillarity term which adds to the standard Fourier contribution, with k the thermal conductivity of the fluid (as for the viscosity, in general, a function of both density and temperature). It's worthwhile noticing that, at variance

with other two–phase models, the diffuse interface approach allows the description of both phases with the same fields. In other words, it does not require the specification of two different velocity or density fields for the two distinct phases; the density field itself allows to distinguish the regions with vapor from those with liquid.

2.2. Fluctuating hydrodynamics theory

The DI approach is able to capture only some of the phenomena occurring at the mesoscale level. The description provided by the model is in fact deterministic, which is a good approximation when the focus is on the larger hydrodynamic scale (larger than few microns at least) of the entire two–phase flow. Close to the length scale of the interface, however, thermal fluctuations become relevant requiring a stochastic description of the system (Buff et al., 1965; Sanyal et al., 1991; Sides et al., 1999). The Fluctuating Hydrodynamics (FH) theory, originally proposed by Landau and Lifshits (L&L) (Landau and Lifshits, 1959) and later developed in several works such as (Fox and Uhlenbeck, 1970; Español, 1998; Rubı and Mazur, 2000; Sengers and de Zárate, 2007), introduces thermal fluctuations in the continuum framework described by the Navier–Stokes equations for simple fluids. L&L's idea was to treat the thermodynamic fluxes, namely, stress tensor and energy flux, as stochastic processes whose statistical properties can be inferred by enforcing the fluctuation-dissipation balance (FDB). Dissipation in fluids, in fact, can be seen as the macroscopic manifestation of the energy transfer arising from random molecular interactions. As a consequence dissipation and fluctuations must be linked together by a suitable FDB. The original L&L theory deals with linear fluctuations around equilibrium states but the theory has been generalized to linear fluctuations around non-equilibrium steady states (Tremblay et al., 1981). More recently FH has been extended to capillary fluids (Shang et al., 2011) to study the spinodal decomposition induced by thermal noise (Chaudhri et al., 2014), and was exploited to study interface fluctuations near the contact line (Belardinelli et al., 2016) and the nucleation of cavitation bubbles (Gallo et al., 2018; 2020). The application of the FDB to unsteady non-equilibrium states is justified when a separation of timescales between slow variables (the hydrodynamic conserved variables, for example) and fast variables (positions and momenta of the molecule constituting the fluid system) occurs. In nucleation phenomena, for example, the typical waiting time to observe the nucleation event is much longer than the molecular timescale, hence the hydrodynamic variables are reasonably slower than the molecular agitation. A rigorous derivation of the non-linear fluctuating model, to be applied to unsteady non-equilibrium conditions, has been proposed in (Zubarev and Morozov, 1983; Español, 1998), within the framework of Fokker-Plank descriptions. Again, the main assumption in the derivation is the clear separation of timescales.

Here we summarize the main aspects of the model and refer the interested reader to Gallo et al. (2018) for the detailed derivation through the application of the FDB, and to Español (1998) for the derivation via the Fokker-Plank description. The stochastic evolution of the two–phase system is described by the conservation laws in Eq. (4) supplemented with the stochastic forcing terms in the momentum and energy equations:

$$\begin{aligned}
\frac{\partial \rho}{\partial t} + \boldsymbol{\nabla}\cdot(\rho\mathbf{u}) &= 0\,,\\
\frac{\partial \rho\mathbf{u}}{\partial t} + \boldsymbol{\nabla}\cdot(\rho\mathbf{u}\otimes\mathbf{u}) &= \boldsymbol{\nabla}\cdot\boldsymbol{\tau} + \boldsymbol{\nabla}\cdot\tilde{\boldsymbol{\tau}}\,,\\
\frac{\partial e}{\partial t} + \boldsymbol{\nabla}\cdot(\mathbf{u}e) &= \boldsymbol{\nabla}\cdot[(\boldsymbol{\tau}+\tilde{\boldsymbol{\tau}})\cdot\mathbf{u}] + \\
&\quad -\boldsymbol{\nabla}\cdot(\mathbf{q}+\tilde{\mathbf{q}})\,,
\end{aligned} \tag{5}$$

where $\tilde{\boldsymbol{\tau}}$ is the stochastic stress tensor, expressed in terms of a delta-correlated white noise symmetric tensor $\boldsymbol{\eta}(\mathbf{x}, t)$, whose components are

$$\tilde{\tau}_{ij} = \sqrt{2k_B\theta\mu}\left[\eta_{ij} - \delta_{ij}\frac{1}{3}\eta_{kk}\right], \tag{6}$$

with k_B the Boltzmann constant, δ_{ij} the Kronecker delta and with

$$\begin{aligned}
\langle\eta_{ij}(\mathbf{x},t)\rangle &= 0\,,\\
\langle\eta_{ij}(\mathbf{x},t)\eta_{i'j'}(\mathbf{x}',t')\rangle &= \left(\delta_{ii'}\delta_{jj'} + \delta_{ji'}\delta_{ij'}\right)\delta(\mathbf{x}-\mathbf{x}')\delta(t-t')\,.
\end{aligned}$$

Similarly $\tilde{\mathbf{q}}$ is the stochastic heat flux, expressed in terms of another delta-correlated white noise $\boldsymbol{\zeta}(\mathbf{x}, t)$, with components

$$\tilde{q}_i = \sqrt{2k_B\theta^2 k}\zeta_i\,, \tag{7}$$

with

$$\begin{aligned}
\langle\zeta_i(\mathbf{x},t)\rangle &= 0\,,\\
\langle\zeta_i(\mathbf{x},t)\zeta_{i'}(\mathbf{x}',t')\rangle &= \delta_{ii'}\delta(\mathbf{x}-\mathbf{x}')\delta(t-t')\,.
\end{aligned}$$

It's worthwhile noticing that, as a result of the FDB, the above expressions of the stochastic fluxes are linked to the viscosity and the thermal conductivity coefficients, which modulate the intensity of the dissipation mechanisms in the fluid: the higher is the dissipation (large viscosity or large thermal conductivity), the larger is the resulting stochastic forcing.

One of the major feature of the set of stochastic equations, Eqs. (5), is its ability to sample the hydrodynamics fields fluctuations at equilibrium. The static correlation functions of a thermodynamic system in equilibrium can be evaluated from the entropy deviation from its equilibrium value. It is possible to show (Gallo et al., 2018) that for a capillary fluid described by the free energy functional in Eq. (1), the density, velocity and temperature are Gaussian random fields with the following equilibrium two-points, two-times, correlations:

$$\begin{aligned}
\langle\rho(\mathbf{x},t)\rho(\mathbf{x}',t')\rangle &= \frac{k_B\theta_{eq}}{4\pi\lambda|\mathbf{x}-\mathbf{x}'|}\delta(t-t') \\
&\qquad \exp\left[-|\mathbf{x}-\mathbf{x}'|\sqrt{\frac{c_{eq}^2}{\lambda\rho_{eq}}}\right], \qquad (8)\\
\langle\mathbf{u}(\mathbf{x},t)\otimes\mathbf{u}(\mathbf{x}',t')\rangle &= \frac{k_B\theta_{eq}}{\rho_{eq}}\boldsymbol{I}\delta(\mathbf{x}-\mathbf{x}')\delta(t-t')\,,\\
\langle\theta(\mathbf{x},t)\theta(\mathbf{x}',t')\rangle &= \frac{k_B\theta_{eq}^2}{\rho_{eq}c_v}\delta(\mathbf{x}-\mathbf{x}')\delta(t-t')\,. \qquad (8)
\end{aligned}$$

In the above equations the subscript eq refers to the equilibrium properties, $\mathbf{x}$ and $\mathbf{x}'$ are two points in the fluid domain, t and t' two time instants, $c^2 = \partial p/\partial\rho|_\theta$ is the isothermal speed of sound, and c_v is the specific heat capacity at constant volume. It worths noticing that the exponential spatial correlation of density fluctuations arise from the long range capillary interactions and is not spatially delta-correlated as usual in simple fluids (De Zarate and Sengers, 2006).

2.3. Boundary conditions for boiling problems

The set of Eq. (5) has to be supplemented with suitable boundary conditions to address the boiling phenomenon. In this work we will focus on saturated pool boiling conditions, where the liquid is kept at saturation close to a heated surface. To enforce the saturated ambient conditions, the temperature θ_{ext} and the pressure $p_{ext} = p_{sat}(\theta_{ext})$ have to be prescribed at infinity, or more practically very far from the wall. On the wall the value of the heat flux, $\mathbf{q}\cdot\mathbf{n} = q$, is specified to constantly heat up the surface, and the classical no-slip and impermeable condition, $\mathbf{u} = 0$, is assigned

for the velocity field. The DI model mathematically requires a condition for the normal derivative of the density at the wall (Jamet et al., 2001; Seppecher, 2000). On a physical ground this condition is associated with the wetting properties of the solid surface, namely the contact angle (Thomas and McGaughey, 2007). In this work we will focus on neutrally wetting surfaces (i.e. 90° contact angle) which is equivalent to prescribe a homogeneous Neumann condition on the density, $\partial\rho/\partial n = 0$. The effect of different wettabilities will be addressed in future works, by generalizing the boundary prescription proposed by Cahn (1977) in the context of the Cahn-Hilliard model.

3. Algorithms & solution techniques

3.1. Simulations setup

The bulk thermodynamic properties of the fluid are here described through the van der Waals Equation of State. It worths noticing that the DI model could be exploited with more sophisticated equations that could better describe the properties of a given particular fluid of interest. For example, the Equation of State for a Lennard–Jones fluid (Johnson et al., 1993) or for water (Kestin et al., 1984) could be adopted. The van der Waals fluid, however, represents a good compromise attaining the crucial features of a vapor–liquid system but with a low level of complexity.

All quantities in the following text and in the figures are made dimensionless by using the critical properties of the fluid as reference values, as commonly done with the van der Waals equation of state: $p^* = p/p_c$, $\theta^* = \theta/\theta_c$, $\rho^* = \rho/\rho_{ref}$, $x^* = x/L_{ref}$, $t^* = t/t_{ref}$ are the non-dimensional pressure, temperature, density, spatial coordinate and time, respectively. Here we will refer to the critical values of water, whose critical pressure is $p_c = 22\,\mathrm{MPa}$ and whose critical temperature is $\theta_c = 647\,\mathrm{K}$. The other reference values are obtained accordingly: the critical density is $\rho_{ref} = 8p_c/(3R_w\theta_c) = 196.8\,\mathrm{kg/m^3}$ with $R_w = 461.5\,\mathrm{J/(kg\,K)}$ the specific gas constant of water, the reference length $L_{ref} = (k_B\theta_c/p_c)^{1/3} = 0.74\,\mathrm{nm}$, the reference velocity is $V_{ref} = (p_c/\rho_{ref})^{1/2} = 334.8\,\mathrm{m/s}$, the reference time is $t_{ref} = L_{ref}/V_{ref} = 2.21\,\mathrm{ps}$, and the reference heat flux is $q_{ref} = p_cV_{ref} = 7.356\,\mathrm{GW/m^2}$. The fitted laws for dynamic viscosity $\mu(\rho, \theta)$ and thermal conductivity $k(\rho, \theta)$ proposed by the International Association for the Properties of Water and Steam (IAPWS) in Kestin et al. (1984) are also used, in order to mimic the density and temperature dependence of viscosity and thermal conductivity in water. Hereafter in the text and in the figures we will only refer to the dimensionless quantities defined above, except when explicitly mentioned, and we will avoid the use of the symbol * for the ease of notation. In dimensionless form the van der Waals Equation of State reads:

$$f_b(\rho,\theta) = \frac{8\theta\rho}{3\delta} - 3\rho^2 + \frac{8}{3}\theta\rho\log\left(\frac{\rho}{3-\rho}\right), \tag{9}$$

where $\delta = R_w/c_v$, with c_v the specific heat at fixed volume, being $0 < \delta \leq 2/3$, with $\delta = 2/3$ for monoatomic fluids (Zhao et al., 2011). Here $\delta = 0.112$ is chosen to recover a realist specific heat for water. Finally, the value of the capillary coefficient $\lambda = 5.3 \times 10^{-16}\,\mathrm{m^7/(s^2kg)}$ has been chosen in order to reproduce the surface tension of water $\gamma = 0.072\,\mathrm{N/m}$ at ambient temperature, through Eq. (2). The corresponding interface thickness obtained through Eq. (3) is $\epsilon = 1.3\,\mathrm{nm}$, comparable with the experimental value $\epsilon = 1\,\mathrm{nm}$ measured via ellipsometry in (Kinosita and Yokota, 1965). When increasing the temperature, the surface tension and the interface thickness are expected to decrease and increase, respectively. For example, at non-dimensional temperature $\theta = 0.9$, the values $\gamma = 0.006\,\mathrm{N/m}$ and $\epsilon = 3.4\,\mathrm{nm}$ are obtained.

The simulated system consists in a cubic domain, with length $L = 500$ with a solid wall on the bottom boundary ($z = 0$) and an open boundary in $z = L$ where both the temperature and the pressure are assigned. Non-reflecting boundary conditions are enforced on the open boundary to avoid the reflection of the pressure waves in the fluid domain (Poinsot and Lele, 1992; Delgado-Buscalioni and Dejoan, 2008). Periodic boundary conditions are imposed in x and y directions. The initial conditions correspond to a uniform and quiescent liquid at the saturation temperature $\theta_0 = 0.9$, $p_0 = p_{sat}(\theta_0) = 0.647$, $\rho_0 = \rho_{Lsat}(\theta_0) = 1.657$. The system of equations, Eqs. (5), has been discretized in the spirit of the method of lines with the same numerical scheme already adopted and validated in Gallo et al. (2018). Briefly, a uniformly spaced staggered grid, with 100x100x100 cells, has been used to spatially discretize the equations, following Balboa et al. (2012). Due to staggering, scalar fields, e.g., density, are located at the cell center, while components of vector fields in a given direction are located at the center of the perpendicular face. The time evolution has been performed by means of a second-order Runge-Kutta scheme (Delong et al., 2013), with a constant timestep $\Delta t = 0.01$.

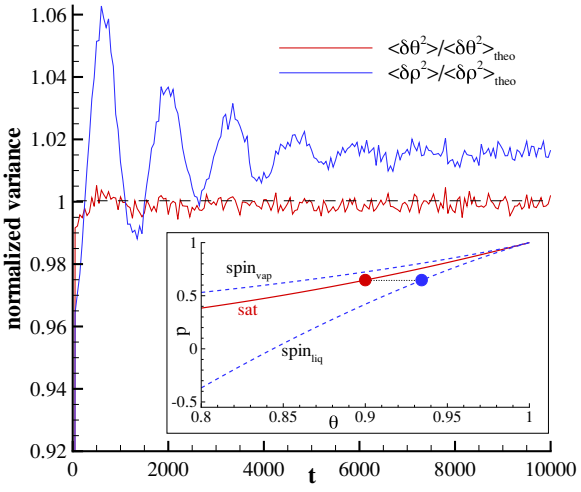

Fig. 1. Evolution of normalized density (blue curve) and temperature (red curve) variances during the thermal equilibration pre-process. Statistical equilibrium is reached after time $t = 6000$ and the configuration at $t = 10000$ has been used as initial condition for the subsequent boiling simulations. In the inset the phase diagram for the van der Waals equation of state is reported in the $p - \theta$ plane. Both the vapor-liquid saturation curve (red solid line) and the spinodal curves (blue dashed lines) are reported. The red dot corresponds to the saturation thermodynamic condition chosen for the present analysis, at $\theta = 0.9$, and the blue dot represents the spinodal limit for bubble nucleation, at $\theta = \theta_{spin} \simeq 0.935$. (For interpretation of the references to color in this figure legend, the reader is referred to the web version of this article.)

Before starting the actual boiling simulations, a first preprocessing step is performed for thermostatting the fluid, with the thermal noise forcing the liquid system and producing the thermal fluctuations: the temperature $\theta = \theta_0$ is applied on both bottom and top boundaries and the saturation pressure $p = p_0$ is applied only on the open boundary. The variance of temperature and density fluctuations are monitored during the process and the simulation is stopped when they reach a stable value, indicating that the statistical equilibrium is reached. In Fig. 1 we report the evolution of normalized variances up to the statistical equilibrium condition. The theoretical values for temperature and density variances in Eq. (8) are used to normalize the numerical values. At equilibrium the fluctuations recover the theoretical variances with an error lower than 2%, common in FH simulations (Gallo et al., 2018). The statistical equilibrium configuration reached is used as the initial condition for all the following boiling simulations. In the inset of Fig. 1 we reported the phase diagram for the chosen van der Waals equation of state, in the $p - \theta$ plane. In particular we highlighted the Clausius-Clapeyron, vapor-liquid, satura-

tion curve (in solid red) and the two spinodal curves (dashed blue) representing the thermodynamic limit for nucleation. The red dot represents the saturation condition chosen for the simulations, at $\theta = 0.9$, and the blue dot represents the spinodal limit for bubble nucleation, at $\theta = \theta_{spin} \simeq 0.935$ (also known as the bulk thermodynamic limit of superheat, far from the wall (Carey, 2018)). The boiling onset would be expected in this range of metastable conditions. The particular choice of the thermodynamic condition here analyzed worths a further comment. Both FH theory and DI model are extremely general and can be applied in principle in all thermodynamic conditions, even closer to more realistic temperatures in common experiments. However, their implementation in a numerical scheme must cope with technical difficulties associated with, for example, the huge vapor–liquid density ratio occurring at lower temperatures. These technical complexities would not add any crucial features to the physical description of the boiling inception phenomenon, but would have considerably increased the computational cost. Hence, the choice of the particular condition $\theta = 0.9$ where $\rho_{Lsat}/\rho_{Vsat} \simeq 4$ is a non negligible but still manageable density ratio.

The subsequent boiling simulations consist in a set of different (statistically independent) runs where we applied the same constant value of the heat flux, q, on the solid wall. In each of these runs we used a different value of the seed employed to generate the random white noises in Eq.s (6,7). Each simulation hence corresponds to a sample of the non-stationary stochastic process leading to bubble inception. As opposed to the analysis of statistically stationary problems, where the ergodic hypothesis is widely used to replace the proper ensemble average with a time average, here the time dependent statistically relevant results are obtained through the ensemble averages, at fixed time, over all the sample simulations performed. At each heat flux condition analyzed, 40 samples have been used to obtain well converged statistical results.

3.2. Bubble detection algorithm

The identification of the distinct bubbles in the code is based on classical clustering algorithms. 1) The first step is a *cell-flagging procedure* that selects the grid cells to be considered as vapor based on the local density value. The critical density ρ_{ref} is a reasonable cut-off value, hence all the grid cells with a non-dimensional density value $\rho < 1$ are flagged as vapor cells. 2) A clustering technique based on a region growing procedure is applied to the flagged vapor cells. This approach examines neighboring cells of a given vapor cell and determines whether the neighbors should be added to the aggregate. The process is iterated until all the detected vapor cells have been clustered into distinct aggregates. 3) The properties of each vapor aggregate is then evaluated. As an example, the volume of the kth aggregate is obtained as the sum of the flagged grid cell volumes composing the kth cluster. All the aggregates constituted by a single vapor cell are disregarded in the analysis since they would have introduced ambiguity in the subsequent tracking procedure: in situations where a single vapor cell is close to a larger aggregate at time t_1 and disappears at time $t_1 + \Delta t$ it is not possible to distinguish if the single-cell aggregate merged with the larger one or if it has been reabsorbed in the liquid phase while the larger aggregate grew by one cell. When transposed to larger aggregates this ambiguity resolves since it is very unlikely that a large aggregate is reabsorbed altogether during a single timestep. Together with the volume we collected the area of contact with the solid surface, the mean density and the coordinates of the center of mass, for each vapor aggregate. The technique proposed in Bai and Breen (2008) is exploited to cope with the periodic boundary conditions in x and y directions for the proper calculation of the center of mass.

The detection algorithm is performed at each time instant. Finally a tracking procedure is applied to follow the time evolution of each aggregate. Both the center of mass position and the radius are used to correlate the vapor aggregates at two consecutive time instants. The procedure allows to obtain the complete trajectory in space and the size evolution of each vapor aggregate, but also to identify any possible coalescence event.

4. Results and discussions

Fig. 2 shows some configurations of the vapor bubbles during the boiling process with a constantly applied heat flux, $q = 0.01$. After a waiting period characterized by the appearance/disappearance of small vapor embryos, the wall reaches a suitable temperature that triggers the nucleation: fluctuations in the liquid produce vapor regions large enough to overcome the activation barrier and grow. The growth process is characterized by a coupled expansion-coalescence mechanism (see the snapshots (c) and (d), for example) that leads to the formation of a vapor layer over the hot wall (snapshot (f)).

Fig. 3 shows the time evolution of the temperature averaged on the wall, $\langle\theta_{wall}\rangle$, with different heat flux values. At lower heating levels the wall will require a longer time to reach the nucleation temperature and, consequently, the bubbles will appear at later times. After nucleation, the bubble growth process removes energy from the hot wall (due to the latent heat of evaporation) and the mean temperature decreases. At higher heat flux, when q is comparable with the heat removal associated with the bubble growth, this temperature decrease is reduced. Since the system analyzed here is small, a vapor layer forms when all the bubbles have coalesced together, sort of insulating the wall (see Fig. 2(f)). This is the reason why the wall temperature starts increasing again, in all the cases analyzed. The curves in Fig. 3 allow to detect the onset temperature of boiling (i.e. the nucleation temperature), θ_{ons}, as the wall mean temperature when the first local maximum is reached. Please notice that this definition differs from those based on thermodynamic and kinetic reasonings, for example those defined within the Classical Nucleation Theory (Carey, 2018), or those based on the cavity theory (Hsu, 1962). In fact, both these theories relate to the knowledge of the critical embryo dimension as a function of superheat and defect dimensions on the surface. Moreover they apply to idealized nucleation conditions of isolated and non-interacting bubbles and do not take into account any dynamical effect. As discussed in the introduction, on ideally smooth surfaces these theories would produce expected nucleation temperature close to the spinodal temperature. On the contrary experiments showed that even on ultra-smooth surfaces, with surface roughness on the nanometer scale, the temperature of boiling incipience is extremely lower than the expected theoretical value (Bourdon et al., 2012). Being based on an average temperature on the surface, the operative definition adopted here is closer to what is available from experiments, where the sensor averages the information on a larger length scale (compared to the nano-micro meter scale of the single critical embryo) and where the onset temperature is associated to the optical detection of a bubble whose dimension is orders of magnitude larger than the critical embryo. Moreover the definition here adopted takes into account the complex boiling phenomenon in its entirety, being the result of the interaction between all the growing bubbles. In all the heating level conditions here analyzed the nucleation temperature is lower with respect to the spinodal temperature (in these conditions $\theta_{spin} \simeq 0.935$). Moreover θ_{ons} increases together with the provided heat flux (see the inset of Fig. 3), a dependence which is impossible to predict with a static approach such as the CNT. We correlated the available data and a power law properly fit the simulations results. This could allow to extrapolate the nucleation

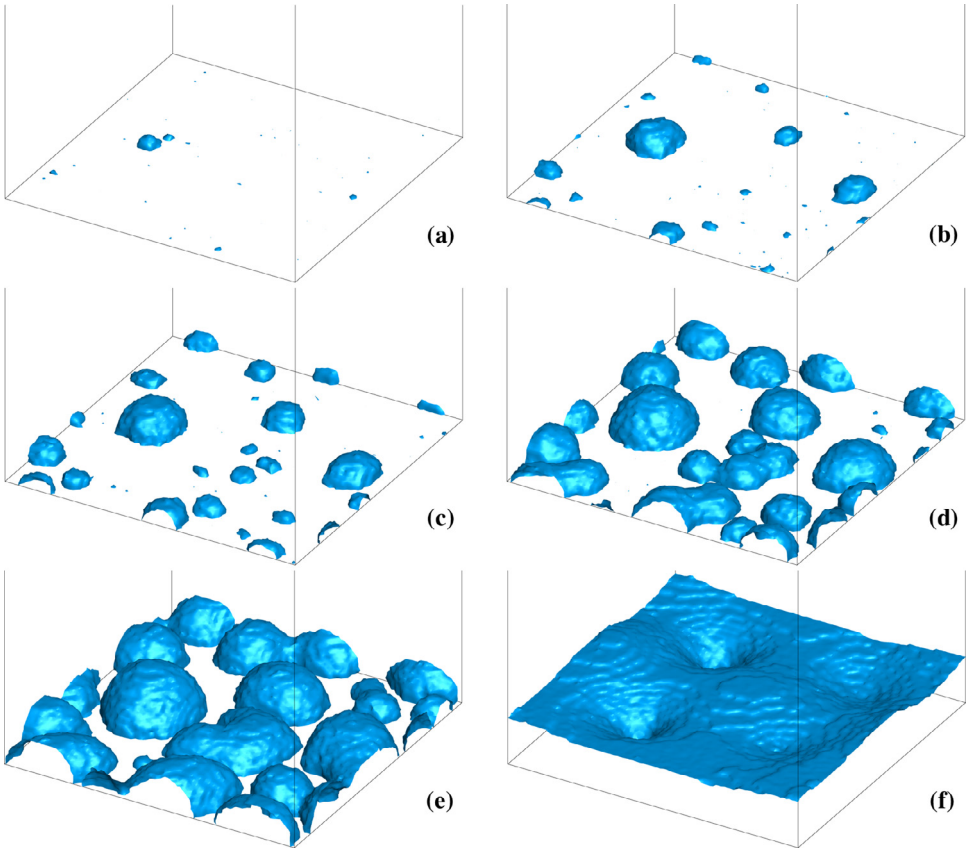

Fig. 2. Vapor bubble evolution during nucleate boiling with the heat flux $q = 0.01$. The figures refer to one sample randomly extracted from the set of different simulations in the same condition. Letters from (a) to (f) represent the time instants: (a) $t = 16500$, (b) $t = 17500$, (c) $t = 18000$, (d) $t = 19000$, (e) $t = 20000$, (f) $t = 24500$.

temperature at typical experimental heat flux values (smaller q). In fact, typical values of few MW/m^2 correspond to non dimensional q values on the order of $10^{-4} - 10^{-3}$. Simulations at such small values are hardly affordable even with this technique, since it would require too much time to observe the nucleation.

To substantiate more on the heat removal effect due to bubble growth, we plot in Fig. 4 a comparison between the input power $W_{in} = qA$, with A the area of the heated surface, and the estimated power required for phase change, W_{pc}. This power is evaluated as $W_{pc} = \dot{M}_{vap}\ell$, with $\dot{M}_{vap}$ the time derivative of the mass of vapor in the system, and ℓ the latent heat of evaporation at temperature $\theta = 0.92$, close to the wall mean temperature at nucleation. It is worth noticing that the choice of a representative homogeneous temperature close to the nucleation temperature is enough for the purpose of this estimate notwithstanding the actual temperature is non-homogeneous both in space and in time. In the plot the grey area represents the time interval when the mean temperature of the system (plotted with the black curve) decreases, and almost corresponds to the region where $W_{pc} > W_{in}$, confirming that the temperature reduction is due to the evaporation process. In Fig. 4 we analyzed two different values of the heat flux, $q = 0.01$ on the left and $q = 0.02$ on the right, and we obtained similar results in both conditions. By comparing the level of W_{pc} in the two plots we observe that the vapor formation is more impulsive at higher heat flux values, as expected.

A more microscopic analysis of the boiling onset process can be performed by tracking the dynamics of each single vapor aggregate. In the following we will adopt the classical nomenclature in the field of bubble nucleation to distinguish the different vapor aggregates as a function of their size: we will refer to *embryos* when the aggregate is small, more precisely smaller than the critical size to be defined later in this section; we instead call them *bubbles* when they are larger than the critical size. By following each embryo it is possible to distinguish those fluctuations that actually lead to the formation of a bubble, from those which are not intense enough and do not trigger the evaporation. This kind of analysis is formalized, in the more general context of activated processes, after the introduction of the concepts of reaction coordinate, isocommittor surface and transition state (Weinan et al., 2005), see Appendix A for details. When applied to boiling onset, the most widely used reaction coordinate is the embryo radius and the transition state corresponds to the critical radius, R_c. CNT, for example, determines the critical radius based on energy considerations only, neglecting any dynamical effect and any bubble-bubble interaction, which have been proved crucial, instead (Marchio et al., 2019; Gallo et al., 2018). Our numerical experiments, on the contrary, take all these effects under consideration and allows a more detailed analysis of the entire transition process. By following the procedure described in Appendix A, the transition probability associated with each bubble dimension has been evaluated and plotted in Fig. 5, for the case with the heat flux $q = 0.01$. As expected, only a small part of those bubbles that reach small radius values during their dynamics are able to reach large dimensions at the late stage of the process. Most of them, in fact, are “re-absorbed” in the liquid phase and disappear. The transition state is determined as the radius associated with 50% probability of transition, resulting in $R_c = 5.9$ by linearly interpolating the available data. Interestingly, the analysis evidences the importance of the coalescence events on the success rate of evaporation: almost two thirds of the reactive trajectories belong to bubbles that experienced merging events during their dynamics. Coalescence, in fact, even between two very small embryos, extends the life of the vapor re-

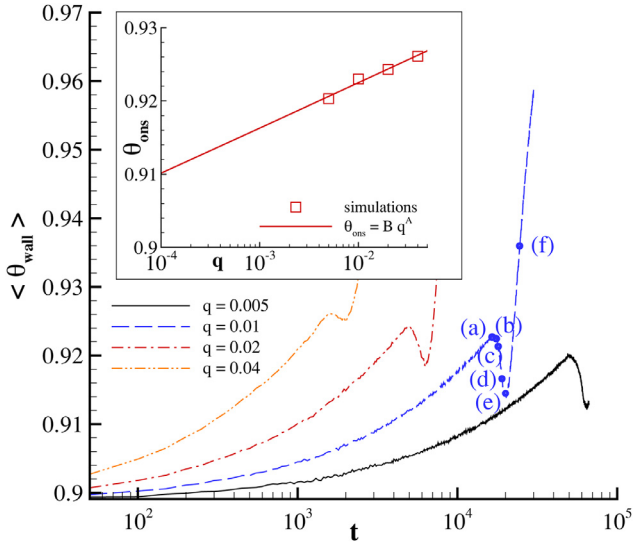

Fig. 3. Time evolution of the mean wall temperature at different heat flux values. The first local maximum corresponds to the appearance of the first large vapor clusters, and represents the nucleation temperature, θ_{ons}. The symbols and the letters superimposed on the blue curve ($q = 0.01$) corresponds to the snapshots shown in Fig. 2. The inset reports the onset temperature as a function of the heat flux, with the red square symbols. A power law properly fit the results, with the coefficient $A = 2.926 * 10^{-3}$ and $B = 0.935$. (For interpretation of the references to color in this figure legend, the reader is referred to the web version of this article.)

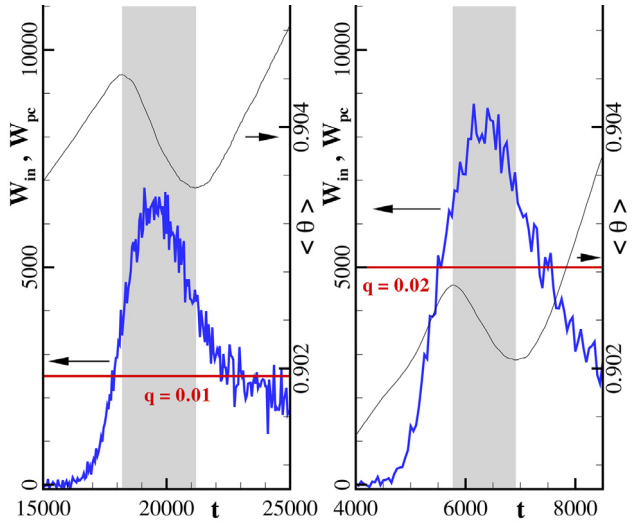

Fig. 4. Comparison of the input power W_{in} (constant red line) and the estimated power required for evaporation W_{pc} (solid blue curve), see text for definitions. The left panel corresponds to the case with $q = 0.01$; the right panel to $q = 0.02$. In both the panels, the grey area represents the time interval during which the mean temperature of the system (plotted with the light black curve) decreases, and almost corresponds to the region with $W_{pc} > W_{in}$. (For interpretation of the references to color in this figure legend, the reader is referred to the web version of this article.)

gion and increases the probability to experience a more intense fluctuation that eventually drives the system to locally evaporate. The results at different values of the heat flux are summarized in Tab. 1, where the wall mean temperature at the time instant of the first appearance of a supercritical bubble ($R > R_c$), θ_{Rc}, is compared with the onset temperature θ_{ons} defined above and in Fig. 3, and with the onset temperature predicted by CNT, θ_{CNT}, when using the measured value of R_c as the critical radius in the theory. The results, expressed in terms of the relative superheat defined as $(\theta - \theta_{sat})/(\theta_{spin} - \theta_{sat})$, apparently show the overestimated prediction provided by the CNT. Moreover the simulations show that

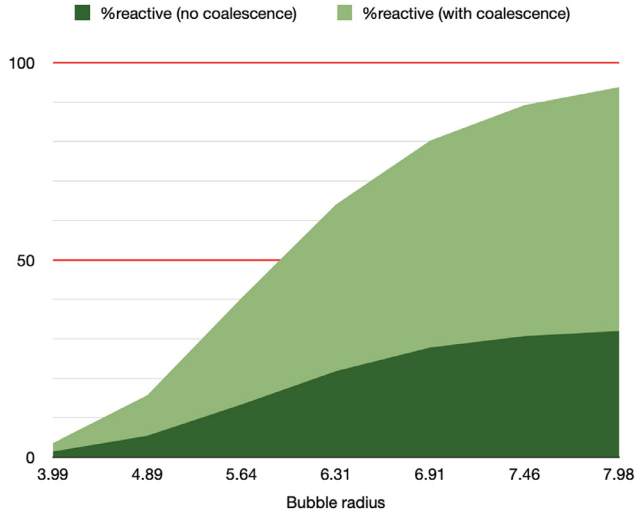

Fig. 5. Transition probability as a function of the embryo radius in the case $q = 0.01$. Among the reactive trajectories, those bubbles that do not experience any coalescence event during their dynamics are reported in dark green in the area chart. The percentage of those who merged with other bubbles at least once, is reported in light green. The effective critical radius, $R_c = 5.9$, is associated with a transition probability of 50%. (For interpretation of the references to color in this figure legend, the reader is referred to the web version of this article.)

Table 1
Measured effective critical radius, R_c, obtained with the 50% transition probability criterion, at different heat flux conditions. The table also compares the different boiling onset temperature definitions: θ_{Rc} is the wall mean temperature measured when the first supercritical bubble appears in the system; θ_{ons} is the measured wall mean temperature when the first local temperature maximum is reached; θ_{CNT} is the estimated CNT onset temperature when using R_c as the critical radius. All the temperature values are re-expressed in terms of relative superheat.

q	R_c	$\frac{\theta_{Rc} - \theta_{sat}}{\theta_{spin} - \theta_{sat}}$	$\frac{\theta_{ons} - \theta_{sat}}{\theta_{spin} - \theta_{sat}}$	$\frac{\theta_{CNT} - \theta_{sat}}{\theta_{spin} - \theta_{sat}}$
0.005	6.4	0.611	0.611	0.805
0.01	5.9	0.646	0.657	0.85
0.02	5.45	0.646	0.696	0.89
0.04	5.12	0.68	0.752	0.92

the different values of q influence the effective critical radius: at higher heat fluxes the boiling process is activated by smaller embryos but larger wall temperature. This point could be thought as a result of the different velocity of the boiling phenomenon induced by the different values of the heat flux. At higher q the wall is heated faster and the vapor embryos have less time to grow by random fluctuations, hence a larger temperature is reached with the embryos still of small size. On the contrary, at lower heat fluxes, the wall temperature increases slowly compared to the time required for a fluctuation to produce a larger embryo; in this condition more embryos of larger size can populate the surface before eventually boil.

The proposed numerical technique allows also the evaluation of the bubble spatial distribution on the wall, thanks to the large number of nucleation events occurring simultaneously in the extended simulated domain. The hypothesis exploited in the CNT, where the nucleation event is rare enough to be considered as an isolated process, would lead to a uniform spatial distribution of the nucleated bubbles. At variance with this expectation, a different nucleation mechanism has been proposed in Uline and Corti (2007) who described the bubble formation as an *activated instability*: vapor embryos surmounting the free energy barrier initiate a local instability that trigger new phase transitions in the

neighboring liquid. This would produce regions of clustered nucleated bubbles, alternated to regions without nucleation events. One of the technical tools to quantify how the bubbles are spatially distributed is the radial distribution function (rdf), $g(r)$. As common in statistical mechanics for a system of particles, the rdf is here used to measure how the density of vapor bubbles varies as a function of the distance from a reference embryo. If $n = N/A$ is the average number density of embryos on the wall (with N the total number of embryos and A the solid surface area), $ng(r)$ represents the local density at distance r. As a consequence, the distribution is uniform if $g(r) = 1$ for every r, while it measures spatial inhomogeneities when $g(r) \neq 1$. In particular $g(r) > 1$ corresponds to region of clustered bubbles. From the operative standpoint, at any given configuration we applied the algorithm for the vapor embryo detection as explained in Section 3.2 and we measured the area of contact with the wall for each embryo, A_i, and the coordinate of its center of mass, $C_i = (x_i, y_i)$. The rdf is then determined by calculating the distance between all embryo pairs, binning these values into a histogram with bin length Δr, and normalizing with the area of the shell $2\pi r \Delta r$ and with the average density n. As a measure of the embryo pairs distance we here used the gap between the bubble surfaces instead of the center-center euclidean distance, since the bubble size is also important in the definition of *neighboring* bubbles:

$$d_{ij} = r_{ij} - (R_i + R_j)\,, \tag{10}$$

with $R_i = (A_i/\pi)^{1/2}$ the radius of the ith vapor embryo and

$$r_{ij} = \left\{ \left[min(|x_i - x_j|, |(L - |x_i - x_j|)|) \right]^2 + \right. \tag{11}$$
$$\left. + \left[min(|y_i - y_j|, |(L - |y_i - y_j|)|) \right]^2 \right\}^{1/2}$$

the center-center euclidean distance which takes into account the periodic boundary conditions applied in x and y directions. The non-stationarity of the phenomenon complicates the evaluation, since the actual rdf, $g(r, t)$, is also time dependent. Moreover, given the finite size of the simulated system, the number of bubble pairs at each time instant is not large enough to obtain statistical meaningful results, in particular at the beginning of the nucleation process when the number of bubbles is small. However, as discussed in Section 3.1, we performed several statistical independent simulations with the same initial and boundary conditions (same value of the heat flux) and with different seeds for the random number generation of the stochastic forcing, in order to properly sample the statistical properties of the dynamical system. We then evaluated the rdf in each sample, $g_s(r, t)$, at the different times and finally performed an ensemble average, $g(r, t) = \langle g_s(r, t) \rangle$. The resulting rdf, in the case with heat flux $q = 0.01$, is shown in Fig. 6 at two different times during the first stage of the nucleation process. The rdf at both times shows a pick ($g(r) > 1$) at small distances, suggesting that the vapor embryos tend to appear close to each other with a higher probability, in line with a description of the process as an activated instability. This pick is more apparent at later times ($t = 17000$ in the figure), when some of the embryos are larger than the critical dimension. The inset in the first row of Fig. 6 (at time $t = 15000$) shows one of the configuration, randomly extracted among the different samples, with all the vapor embryos mainly confined in a small portion of the hot surface. As the time increases and the bubbles grow, the pick in the rdf is even more apparent from the bubble distribution exemplified in the inset ($t = 17000$).

The rdf is also indirectly related to the probability of coalescence between the bubbles: highly clustered embryos would enhance the chances of collisions, hence substantiating the results of the transition probability discussed in Fig. 5. Similar results are obtained with all the heat fluxes here analyzed.

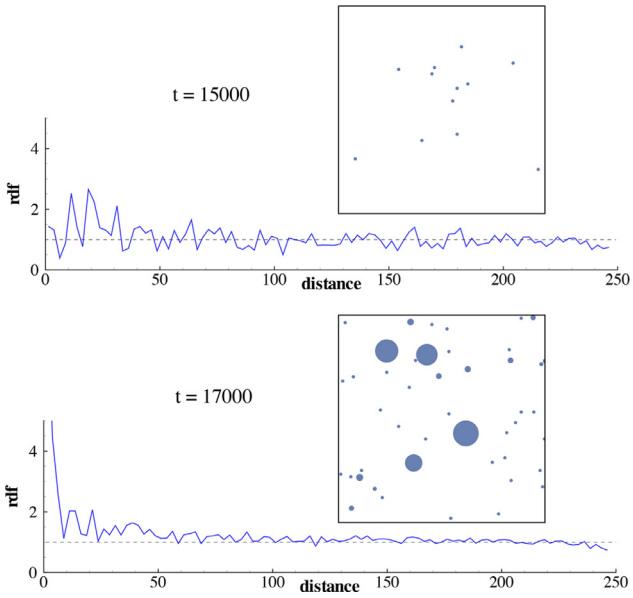

Fig. 6. Radial distribution function at different time instants, in the case with heat flux $q = 0.01$. Each rdf is the average of the distribution of the different samples, at fixed time. The solid blue curve is the rdf calculated using the gap between the bubble surfaces (read the text for the definition); the dashed grey line at $rdf = 1$ represents the case of homogeneously distributed bubbles as a reference. The two insets represent a top view of the bubble configurations, with the blue dots corresponding to the different vapor embryos, where bubble clustering effect is apparent. The size of the dots is reported with the correct proportion between bubble radius and wall size. (For interpretation of the references to color in this figure legend, the reader is referred to the web version of this article.)

5. Conclusions

A numerical investigation of the boiling inception on an ideally smooth surface has been conducted exploiting the Fluctuating Diffuse Interface approach. The analysis evidenced the role of subcritical embryos interaction to enhance bubble nucleation: small vapor embryos are able to survive longer than expected thanks to coalescence events with neighboring embryos. Their longer lifetime increases the probability of experiencing the rare intense thermal fluctuations that triggers the actual bubble formation and the boiling onset. This interaction mechanism is able to support the experimental evidence of very low onset superheat level on ultra-smooth surfaces. In fact, substantially lower superheat, with respect to previous theoretical predictions, have been measured in the present numerical simulations. The formation of bubble clusters have also observed, reinforcing the role of bubble–bubble interactions during the boiling inception process. Moreover the dynamical effect induced by the different values of the heat flux, also plays a role in determining the onset temperature: the faster is the process (at higher value of the heat flux) the less effective is the fluctuation-induced mechanism, since the more intense thermal forcing is able to trigger the boiling at higher wall temperatures.

From the numerical perspective, despite the substantial reduction of computational cost when compared with MD simulations, the proposed methodology still requires strong improvement in order to be further pushed towards the analysis of more application-oriented conditions. As discussed in Section 3, the model is general and robust enough to be applied to different fluids and different thermodynamic conditions, but its implementation in a numerical scheme should address technical difficulties like dealing with high density ratio, or coping with positivity preserving and numerical stability issues associated with fluctuations in vapor at very low densities (Russo et al., 2019).

Finally, the proposed approach proved to be effective in dealing with nucleation processes. At variance with most of the available numerical techniques, where nucleii of the new phase must be patched as initial conditions for the simulations, the Fluctuating Diffuse Interface allows to capture the spontaneous appearance, and the successive growth, of vapor bubbles on the hot surface, thanks to the proper description of thermal fluctuations. This could open new routes for the numerical analysis of more general phase change phenomena.

Declaration of Competing Interests

The authors declare that they have no known competing financial interests or personal relationships that could have appeared to influence the work reported in this paper.

CRediT authorship contribution statement

Francesco Magaletti: Conceptualization, Methodology, Software, Investigation, Writing - original draft, Visualization, Funding acquisition. **Anastasios Georgoulas:** Writing - review & editing, Supervision. **Marco Marengo:** Conceptualization, Writing - review & editing, Supervision.

Acknowledgement

This project has received funding from the European Union's Horizon 2020 research and innovation programme under the Marie Skłodowska-Curie grant agreement No. [836693]. Francesco Magaletti also acknowledges the CINECA award under the Iscra project (project id: IscrB_HET-NUCL), for the availability of high performance computing resources and support.

Appendix A. Statistical tools for the analysis of activated processes

Activated processes such as phase transitions, chemical reactions, wetting and recovery of textured surfaces, or conformational changes of proteins are stochastic processes that drive a system from a stable state A to another stable state B (with A and B representing two local minima of the energy landscape describing the system). During the transition from A to B the system needs to surmount an energy barrier. Pictorially, the energy landscape could be imagined as a mountain landscape, with two valleys separated by a mountain pass: the valleys are the two stable states A and B, while the mountain pass represents the transition state T, the easiest way to go through the mountain although at a higher level with respect to the valleys. From a dynamical point of view a spontaneous transition is very unlikely: thermal fluctuations allow the system to randomly explore the neighborhood of the initial state A, but it would be improbable that a fluctuation will lead it through the state B. The probability of reaching T, and from there transition to B, exponentially decreases with the increase of the energy barrier (as in the Arrhenius law). This is the reason why these events are called *rare events*.

In order to quantitatively analyze these stochastic processes, it is instrumental to introduce the concepts of reaction coordinate and isocommittor surface (Weinan et al., 2005; Bolhuis et al., 2002; Allen et al., 2006; Giacomello et al., 2015). The reaction coordinates are general quantities that allow the description of the transition progress from A to B. Each vector value of the reaction coordinates can be associated with the probability to reach the final state B. An isocommittor surface is an isoprobability surface in the configuration space (the space of the chosen reaction coordinates); in other words, a trajectory launched from any point on one of these surfaces has the same probability to reach the state B. The transition states are defined as those configurations on the isocommittor surface with 50% probability of transition. In fact, being the transition state a saddle point, when the system is exactly at state T it has half the chances to come back to A, and the other half to get to B. The 50% surface formally delimits the configurations that unlikely lead to the state B, from those with a high success rate. The mechanism underlaying the transition can be deduced by following the paths that lead to the transition events (*reactive trajectories*).

When dealing with bubble nucleation (both homogeneous and heterogeneous) the most widely used reaction coordinate is the bubble radius, and the transition state corresponds to the critical radius, as depicted within the CNT (Blander and Katz, 1975; Ward et al., 1983; Debenedetti, 1996; Kashchiev, 2000), associated with the maximum of the system free energy. A trajectory in the phase space of bubble radius is said to be reactive when the vapor embryo reaches the critical size and successively grows indefinitely (or practically, reaches a very large size). The CNT provides an estimate of the critical radius based on energy reasonings only, whilst liquid inertia (Marchio et al., 2019) and bubble-bubble interactions (Gallo et al., 2018) have been proved to affect the mechanism and the probability of transition.

The FDI model proposed here allows the tracking of each embryo during the dynamical process, enabling the collection of several trajectories, namely, the time evolutions of the embryos radius. The isocommittor surfaces are then evaluated by associating each radius value with the probability to reach the "nucleated" state (i.e., a very large size). In other words, the ratio between the number of reactive trajectories and the total number of bubbles that reach a threshold value $\hat{R}$, at least at one time instant during their evolution, is calculated. This transition probability evaluation is reiterated for different $\hat{R}$: a large number of bubbles is expected to reach low values of $\hat{R}$ but, among them, only few will eventually transition and grow indefinitely (committor with low probability); on the contrary, larger values of $\hat{R}$ will be reached by fewer bubbles and most of them will also reach the nucleated state (committor with high probability). The radius associated with 50% transition probability is the effective critical radius, representing the transition state. At variance with the classical exploitation of this methodology, where each trajectory is independent one from each other, here the bubble–bubble coalescence events make the analysis more complex. Particular care must be devoted to the counting of reactive trajectories: if the bubble B_1 has a reactive trajectory and, during its dynamics merges with the bubble B_2, the single trajectory that reaches the final nucleated state counts as two reactive trajectories, since it originates from two initially independent bubbles.

References

Allen, R.J., Frenkel, D., ten Wolde, P.R., 2006. Simulating rare events in equilibrium or nonequilibrium stochastic systems. J. Chem. Phys. 124 (2), 024102.
Bai, L., Breen, D., 2008. Calculating center of mass in an unbounded 2d environment. J. Graph. Tools 13 (4), 53–60.
Balboa, F., Bell, J.B., Delgado-Buscalioni, R., Donev, A., Fai, T.G., Griffith, B.E., Peskin, C.S., 2012. Staggered schemes for fluctuating hydrodynamics. Multisc. Model. Simul. 10 (4), 1369–1408.
Belardinelli, D., Sbragaglia, M., Gross, M., Andreotti, B., 2016. Thermal fluctuations of an interface near a contact line. Phys. Rev. E 94 (5), 052803.
Blander, M., Katz, J.L., 1975. Bubble nucleation in liquids. AlChE J. 21 (5), 833–848.
Bolhuis, P.G., Chandler, D., Dellago, C., Geissler, P.L., 2002. Transition path sampling: throwing ropes over rough mountain passes, in the dark. Annu. Rev. Phys. Chem. 53 (1), 291–318.
Bourdon, B., Bertrand, E., Di Marco, P., Marengo, M., Rioboo, R., De Coninck, J., 2015. Wettability influence on the onset temperature of pool boiling: experimental evidence onto ultra-smooth surfaces. Adv. Colloid Interface Sci. 221, 34–40.
Bourdon, B., Rioboo, R., Marengo, M., Gosselin, E., De Coninck, J., 2012. Influence of the wettability on the boiling onset. Langmuir 28 (2), 1618–1624.
Buff, F., Lovett, R., Stillinger Jr, F., 1965. Interfacial density profile for fluids in the critical region. Phys. Rev. Lett. 15 (15), 621.

Cahn, J.W., 1977. Critical point wetting. J. Chem. Phys. 66 (8), 3667–3672.

Carey, V.P., 2018. Liquid Vapor Phase Change Phenomena: An Introduction to the Thermophysics of Vaporization and Condensation Processes in Heat Transfer Equipment. CRC Press.

Chaudhri, A., Bell, J.B., Garcia, A.L., Donev, A., 2014. Modeling multiphase flow using fluctuating hydrodynamics. Phys. Rev. E 90 (3), 033014.

Cornwell, K., 1977. Naturally formed boiling site cavities. Lett. Heat Mass Transf. 4 (1), 63–71.

De Groot, S.R., Mazur, P., 2013. Non-Equilibrium Thermodynamics. Courier Dover Publications.

De Zarate, J.M.O., Sengers, J.V., 2006. Hydrodynamic Fluctuations in Fluids and Fluid Mixtures. Elsevier.

Debenedetti, P.G., 1996. Metastable Liquids: Concepts and Principles. Princeton University Press.

Delgado-Buscalioni, R., Dejoan, A., 2008. Nonreflecting boundaries for ultrasound in fluctuating hydrodynamics of open systems. Phys. Rev. E 78 (4), 046708.

Delong, S., Griffith, B.E., Vanden-Eijnden, E., Donev, A., 2013. Temporal integrators for fluctuating hydrodynamics. Phys. Rev. E 87 (3), 033302.

Dhir, V., 1998. Boiling heat transfer. Annu. Rev. Fluid Mech. 30 (1), 365–401.

Dhir, V.K., Warrier, G.R., Aktinol, E., 2013. Numerical simulation of pool boiling: a review. J. Heat Transf. 135 (6), 061502.

Diemand, J., Angélil, R., Tanaka, K.K., Tanaka, H., 2014. Direct simulations of homogeneous bubble nucleation: agreement with classical nucleation theory and no local hot spots. Phys. Rev. E 90 (5), 052407.

Español, P., 1998. Stochastic differential equations for non-linear hydrodynamics. Physica A 248 (1–2), 77–96.

Espanol, P., 2001. Thermohydrodynamics for a van der Waals fluid. J. Chem. Phys. 115 (12), 5392–5403.

Fox, R.F., Uhlenbeck, G.E., 1970. Contributions to non-equilibrium thermodynamics. i. theory of hydrodynamical fluctuations. Phys. Fluids (1958–1988) 13 (8), 1893–1902.

Frenkel, J., 1955. Kinetic Theory of Liquids. Dover.

Gallo, M., Magaletti, F., Casciola, C.M., 2018. Thermally activated vapor bubble nucleation: the Landau-Lifshitz–Van Der Waals approach. Phys. Rev. Fluids 3, 053604. doi:10.1103/PhysRevFluids.3.053604.

Gallo, M., Magaletti, F., Cocco, D., Casciola, C.M., 2020. Nucleation and growth dynamics of vapour bubbles. J. Fluid Mech. 883.

Georgoulas, A., Andredaki, M., Marengo, M., 2017. An enhanced VoF method coupled with heat transfer and phase change to characterise bubble detachment in saturated pool boiling. Energies 10 (3), 272.

Giacomello, A., Meloni, S., Müller, M., Casciola, C.M., 2015. Mechanism of the Cassie-Wenzel transition via the atomistic and continuum string methods. J. Chem. Phys. 142 (10), 104701.

Gong, S., Cheng, P., 2013. Lattice Boltzmann simulation of periodic bubble nucleation, growth and departure from a heated surface in pool boiling. Int. J. Heat Mass Transf. 64, 122–132.

Hazi, G., Markus, A., 2009. On the bubble departure diameter and release frequency based on numerical simulation results. Int. J. Heat Mass Transf. 52 (5–6), 1472–1480.

Hsu, Y., 1962. On the size range of active nucleation cavities on a heating surface. J. Heat Transf. 84 (3), 207–213.

Incropera, F.P., Lavine, A.S., Bergman, T.L., DeWitt, D.P., 2007. Fundamentals of Heat and Mass Transfer. Wiley.

Jamet, D., Lebaigue, O., Coutris, N., Delhaye, J., 2001. The second gradient method for the direct numerical simulation of liquid–vapor flows with phase change. J. Comput. Phys. 169 (2), 624–651.

Johnson, J.K., Zollweg, J.A., Gubbins, K.E., 1993. The lennard-jones equation of state revisited. Mol. Phys. 78 (3), 591–618.

Kandlikar, S.G., 2004. Heat transfer mechanisms during flow boiling in microchannels. J. Heat Transf. 126 (1), 8–16.

Kashchiev, D., 2000. Nucleation. Elsevier.

Kestin, J., Sengers, J., Kamgar-Parsi, B., Sengers, J.L., 1984. Thermophysical properties of fluid h2o. J. Phys. Chem. Ref. Data 13 (1), 175–183.

Kimura, T., Maruyama, S., 2002. Molecular dynamics simulation of heterogeneous nucleation of a liquid droplet on a solid surface. Microsc. Thermophys. Eng. 6 (1), 3–13.

Kinosita, K., Yokota, H., 1965. Temperature dependence of the optical surface thickness of water. J. Phys. Soc. Jpn. 20 (6). 1086–1086

Kunkelmann, C., Stephan, P., 2009. Cfd simulation of boiling flows using the volume-of-fluid method within openfoam. Numer. Heat Transf. Part A 56 (8), 631–646.

Landau, L.D., Lifshits, E.M., 1959. Fluid Mechanics, 11. Pergamon Press Oxford, UK.

Lee, J., Son, G., 2017. A sharp-interface level-set method for compressible bubble growth with phase change. Int. Commun. Heat Mass Transf. 86, 1–11.

Lee, R., Nydahl, J., 1989. Numerical calculation of bubble growth in nucleate boiling from inception through departure. J. Heat Transf. 111 (2), 474–479.

Liu, J., Landis, C.M., Gomez, H., Hughes, T.J., 2015. Liquid–vapor phase transition: thermomechanical theory, entropy stable numerical formulation, and boiling simulations. Comput. Methods Appl. Mech. Eng. 297, 476–553.

Lorenz, J., Mikic, B.B., Rohsenow, W.M., 1974. The effect of surface conditions on boiling characteristics. In: International Heat Transfer Conference Digital Library. Begel House Inc..

Lutsko, J.F., 2011. Density functional theory of inhomogeneous liquids. iv. squared–gradient approximation and classical nucleation theory. J. Chem. Phys. 134 (16), 164501.

Lutsko, J.F., 2018. Systematically extending classical nucleation theory. New J. Phys..

Lutsko, J.F., Durán-Olivencia, M.A., 2015. A two-parameter extension of classical nucleation theory. J. Phys. 27 (23), 235101.

Magaletti, F., Gallo, M., Marino, L., Casciola, C.M., 2016. Shock-induced collapse of a vapor nanobubble near solid boundaries. Int. J. Multiph. Flow 84, 34–45.

Magaletti, F., Marino, L., Casciola, C., 2015. Shock wave formation in the collapse of a vapor nanobubble. Phys. Rev. Lett. 114 (6), 064501.

Majumdar, A., Mezic, I., 1999. Instability of ultra-thin water films and the mechanism of droplet formation on hydrophilic surfaces. J. Heat Transf. 121 (4), 964–971.

Marchio, S., Meloni, S., Giacomello, A., Casciola, C.M., 2019. Wetting and recovery of nano-patterned surfaces beyond the classical picture. Nanoscale 11 (44), 21458–21470.

Novak, B.R., Maginn, E.J., McCready, M.J., 2007. Comparison of heterogeneous and homogeneous bubble nucleation using molecular simulations. Phys. Rev. B 75 (8), 085413.

Oxtoby, D.W., Evans, R., 1988. Nonclassical nucleation theory for the gas–liquid transition. J. Chem. Phys. 89 (12), 7521–7530.

Patil, R., Prusa, J.Modest, M.F., Simon, T.W., Ali Ebadian, M. (Eds.), 1991. Numerical solutions for asymptotic, diffusion controlled growth of a hemispherical bubble on an isothermally heated surface 170, 63–70.

Poinsot, T.J., Lele, S., 1992. Boundary conditions for direct simulations of compressible viscous flows. J. Comput. Phys. 101 (1), 104–129.

Qi, Y., Klausner, J.F., 2006. Comparison of nucleation site density for pool boiling and gas nucleation. J. Heat Transf. 128 (1), 13–20.

Rubı, J., Mazur, P., 2000. Nonequilibrium thermodynamics and hydrodynamic fluctuations. Physica A 276 (3), 477–488.

Russo, A., Perez, S. P., Durán-Olivencia, M. A., Yatsyshin, P., Carrillo, J. A., Kalliadasis, S., 2019. A finite-volume method for fluctuating dynamical density functional theory. arXiv:1910.05067.

Sanyal, M., Sinha, S., Huang, K., Ocko, B., 1991. X-ray-scattering study of capillary-wave fluctuations at a liquid surface. Phys. Rev. Lett. 66 (5), 628.

Sengers, J.V., de Zárate, J.M.O., 2007. Thermal fluctuations in non-equilibrium thermodynamics. J. Non-Equilib. Thermodyn. 32 (3), 319–329.

Seppecher, P., 2000. Second-gradient theory: application to Cahn-Hilliard fluids. In: Continuum Thermomechanics. Springer, pp. 379–388.

Shang, B.Z., Voulgarakis, N.K., Chu, J.-W., 2011. Fluctuating hydrodynamics for multiscale simulation of inhomogeneous fluids: mapping all-atom molecular dynamics to capillary waves. J. Chem. Phys. 135 (4), 044111.

Shen, V.K., Debenedetti, P.G., 2001. Density-functional study of homogeneous bubble nucleation in the stretched Lennard-Jones fluid. J. Chem. Phys. 114 (9), 4149–4159.

Sides, S.W., Grest, G.S., Lacasse, M.-D., 1999. Capillary waves at liquid-vapor interfaces: amolecular dynamics simulation. Phys. Rev. E 60 (6), 6708.

Son, G., Dhir, V.K., Ramanujapu, N., 1999. Dynamics and heat transfer associated with a single bubble during nucleate boiling on a horizontal surface. J. Heat Transf. 121 (3), 623–631.

Theofanous, T., Tu, J., Dinh, A., Dinh, T.-N., 2002. The boiling crisis phenomenon: Part I: nucleation and nucleate boiling heat transfer. Exp. Therm Fluid Sci. 26 (6–7), 775–792.

Thomas, J., McGaughey, A., 2007. Effect of surface wettability on liquid density, structure, and diffusion near a solid surface. J. Chem. Phys. 126 (3), 034707.

Tremblay, A.-M., Arai, M., Siggia, E., 1981. Fluctuations about simple nonequilibrium steady states. Phys. Rev. A 23 (3), 1451.

Uline, M.J., Corti, D.S., 2007. Activated instability of homogeneous bubble nucleation and growth. Phys. Rev. Lett. 99 (7), 076102.

Van der Waals, J., 1979. The thermodynamic theory of capillarity under the hypothesis of a continuous variation of density. J. Stat. Phys. 20 (2), 200–244.

Wang, C., Dhir, V., 1993. Effect of surface wettability on active nucleation site density during pool boiling of water on a vertical surface. J. Heat Transf. 115 (3), 659–669.

Ward, C., Johnson, W., Venter, R., Ho, S., Forest, T., Fraser, W., 1983. Heterogeneous bubble nucleation and conditions for growth in a liquid–gas system of constant mass and volume. J. App. Phys. 54 (4), 1833–1843.

Weinan, E., Ren, W., Vanden-Eijnden, E., 2005. Transition pathways in complex systems: reaction coordinates, isocommittor surfaces, and transition tubes. Chem. Phys. Lett. 413 (1–3), 242–247.

Welch, S.W., 1998. Direct simulation of vapor bubble growth. Int. J. Heat Mass Transf. 41 (12), 1655–1666.

Zhao, N., Mentrelli, A., Ruggeri, T., Sugiyama, M., 2011. Admissible shock waves and shock-induced phase transitions in a Van der Waals fluid. Phys.Fluids 23, 086101.

Zubarev, D., Morozov, V., 1983. Statistical mechanics of nonlinear hydrodynamic fluctuations. Physica A 120 (3), 411–467.